EFDA–JET–CP(10)05/30

S. Jachmich, G. Arnoux, S. Brezinsek, S. Devaux, T. Eich, W. Fundamenski,
C. Giroud, H.R. Koslowski, Y. Liang, E. de la Luna, G. Maddison, H. Thomsen
and JET-EFDA Contributors

Power and Particle Fluxes to Plasma-Facing Components in ELM-Mitigated H-Mode Discharges on JET

Power and Particle Fluxes to Plasma-Facing Components in ELM-Mitigated H-Mode Discharges on JET

S. Jachmich[1], G. Arnoux[2], S. Brezinsek[3], S. Devaux[4], T. Eich[4], W. Fundamenski[2], C. Giroud[2], H.R. Koslowski[3], Y. Liang[3], E. de la Luna[5], G. Maddison[2], H. Thomsen[4] and JET EFDA contributors*

JET-EFDA, Culham Science Centre, OX14 3DB, Abingdon, UK

[1]Laboratory for Plasma Physics, Ecole Royale Militaire/Koninklijke Militaire School, EURATOM-Association "Belgian State", Brussels, Belgium, Partner in the Trilateral Euregio Cluster (TEC)
[2]EURATOM-CCFE Fusion Association, Culham Science Centre, OX14 3DB, Abingdon, OXON, UK[3]Institut fuer Plasmaphysik, Euratom Association, D-52425 Juelich, Germany, Partner in the Trilateral Euregio Cluster (TEC)
[4]Max-Planck Institut fuer Plasmaphysik, Euratom Association, Garching, Germany
[5]Laboratorio Nacional de Fusion, Asociacion EURATOM-CIEMAT, Madrid, Spain
** See annex of F. Romanelli et al, "Overview of JET Results", (Proc. 22 nd IAEA Fusion Energy Conference, Geneva, Switzerland (2008)).*

Preprint of Paper to be submitted for publication in Proceedings of the 19th International Conference on Plasma Surface Interactions, San Diego, California, USA. (24th May 2010 - 28th May 2010)

ABSTRACT.
The effect of ELM-mitigation techniques such as the use of magnetic field perturbations, gas fuelling and impurity seeding using nitrogen has been studied. With increasing ELMfrequency the heat flux factor reduces only weakly. The heat flux factor, which has been analysed taking into account ELM-profile broadening and strike point movement and which is proportional to the surface temperature rise due to the heat pulse during the ELM, decreases with confinement and pedestal pressure at the same rate for mitigated ELMs using gasfuelling and magnetic perturbation fields. Only at very high fuelling rates of nitrogen, a drastic drop of the heat flux factor with modest confinement reduction has been found.

1. INTRODUCTION

ELMy H-mode is one of the scenarios foreseen for Q = 10 operating in ITER. The accompanying transient heat loads to the divertor in such plasmas are not only an urgent issue for ITER [1], but also for the metallic wall which is presently under construction at JET [2]. Presently, two materials are under discussion for the divertor in ITER: Carbon Fiber reinforced Carbon (CFC) and tungsten. The large surface temperature rise, T_{surf}, at the divertor targets during the ELMs can cause in the case of carbon cracking and sublimation and in the case of tungsten ablation. A heat pulse onto a solid body leads to an increase of T_{surf}, which is roughly proportional to the energy deposited over the wetted area divided by the square root of the duration of the pulse. In order to characterize the surface temperature rise during the ELM we introduce the heat flux factor η_{ELM}:

$$\Delta T_{surf} \propto \eta_{ELM} = \frac{E_{ELM}}{A_{wetted}\sqrt{t_{dur}}} \tag{1}$$

with E_{ELM} as the energy deposited during the ELM at either the inner or outer divertor target, A_{wetted} as wetted area and t_{dur} as time duration of the ELM. For the ITER targets cracking or melting are expected for heat flux factors above ~40MJ $m^{-2}s^{-1/2}$ [3]. However, uncontrolled ELMs in ITER for the 15MA-scenario have ηELM of about 600MJ $m^{-2}s^{-1/2}$ [4]. To reduce this potential threat for the divertor tiles various ELM-mitigation techniques are under consideration, which aim at achieving higher ELM-frequencies f_{ELM} to benefit from the favorable inverse ELM-energy scaling $dW_{ELM} \propto f_{ELM}^{-1}$, where dWELM is the energy released during the ELM at the pedestal. In recent JET-campaigns Resonant-Magnetic-Perturbation (RMP) fields [5], vertical “kicks” [6], impurity seeding [7] and gas puffing have been compared as active ELM-mitigation techniques.

2. APPLICATION OF EXTERNAL MAGNETIC FIELD PERTURBATION (RMPS)

The JET-tokamak is equipped with four external Error Field Correction Coils (EFCCs), which are mounted at equally spaced toroidal locations. The EFCCs can be operated either in an n = 1 configuration, which leads to a strong core perturbation and can seed locked modes, or in an n = 2 configuration, which provides good edge ergodization. The radial perturbation field BR at the outer

plasma boundary is of the order of 6mT [5].

Experiments have been carried out in low and high triangularity discharges with δ ranging from 0.29 to 0.45 and with the outer strike point placed in the middle of the socalled Load Bearing Septum Replacement plate (LBSRP). It is worth mentioning that the choice of the strike point location, which has poorer pumping and hence higher natural ELMfrequency, was based on diagnostic needs. The experiments reported here have the following plasma parameters: $I_p = 2.0$MA, $B_t = 1.9$ T, $q_{95} = 3.2$, $P_{NBI} = 9.0$MW, $\delta = 0.29$. The EFCCs have been operated in n=1-mode. During the Type-I ELMy H-mode flat top phase of the discharge, the EFCC coils have been energised with currents up to 1.5kA*16 turns. At these plasma currents and input power ELMs appear at a frequency $f_{ELM} \sim 15$Hz and release about $dW_{ELM} \sim 100$kJ, which is about 7.7% of the pedestal energy. During the EFCC-phase the ELM-frequency strongly increases to about 40Hz with dWELM dropping to values which lie within the noise of the signal. As a scan of neutral beam power has revealed, the ELMs remain Type-I ELMs despite their higher frequency and smaller amplitude. The loss of core and edge density during the error field application, often referred to as pump-out effect, is not seen as increased particle flux at the divertor in the inter-ELM phases. In low triangularity discharges, the edge temperature remains constant, which results due to the density pump-out in a degradation of the pedestal pressure and energy confinement. In order to compensate the lost density, a gas scan has been carried out. As can be seen in fig 1, in pulses without EFCCs the density, normalised to the Greenwald density scaling, increases with gas fuelling up to 95% where a degradation of particle confinement prevents further increase of the core density. If the EFCCs are operated, the resulting density at a give fuelling rate is always lower than the reference pulses. The density pump-out is in all present. It was impossible to achieve densities beyond 75% of the Greenwald density.

Due to the cooling of the pedestal during gas fuelling, the pedestal and core energy are lower, leading to a degradation of the confinement, which is illustrated in figure 2, where the $H_{98(y,2)}$-factor derived from the thermal energy is plotted against the Greenwald-fraction. As pointed out earlier, all pulses reported here exhibited a density pump-out and a loss of energy. Consequently the operational space to achieve good confinement at high density in EFCCpulses is smaller and further away from the ITER-target ($H_{98(y,2)} \sim 1.0$ and $f_{Gw)} \sim 0.85$).

Another detrimental effect of EFCC-operation is the distortion of the plasma boundary and a reduction of the wall clearance. In the experiments reported above, Langmuir probes, which are embedded in the outer poloidal limiter, have not indicated an increase of the ELMpeak and inter-ELM particle fluxes. However, this applies only to one specific EFCC-phase and mode of operation. In a dedicated phase scan, where the EFCC-coil polarity was varied such that the pattern of the perturbation field is shifted toroidally by 90^o, an increase of the ELM-peak particle flux arriving at the outboard limiter has been observed. Whether this is due to a reduction of the wall clearance caused by non-axis symmetric plasma distortion or a reaction of the feedback system, which the changes the position of the outer plasma boundary, is currently under investigation.

3. DIVERTOR TARGET PROFILES

A new Infra-Red camera (IR) is viewing the outer strike zone at the JET-divertor. The view of the IR-camera covers the same spatial range as Langmuir Probes (LP), which are embedded into the divertor. The time resolution of the IR was 86μs and that of the LPs 100μs, being sufficient to resolve typical JET Type-I ELMs, which have a rise time of about 100-200μs and a decay time of a few milliseconds. More details on the IR-diagnostic can be found in [8].

The target plate, which is viewed by the IR, is equipped with five triple and five single probes. A fixed negative voltage has been applied to the single probes to determine particle fluxes during ELMs. Every 50ms the probe voltage has been swept to obtain I(V) - characteristics for inter - ELM electron temperature measurements. Fair agreement of surface power fluxes measured by the LPs with those measured by the IR-diagnostic has been found [8]. However, due to the limited spatial resolution the study in this paper has been restricted to particle flux measurements.

Figure 3 shows inter-ELM profiles of surface heat flux measured by IR of an unfuelled pulse during phases with and without EFCCs. The profiles have been obtained by averaging over the inter-ELM periods. First we note the rather narrow inter-ELM profile for the case without EFCC. The width is about 3cm, which corresponds to 5mm at the outer midplane and is in agreement with the results reported in [9]. During the ELM, the deposition profile strongly broadens. This confirms our earlier observation of ELM power flux profile broadening measured by Langmuir probes [10]. With the EFCCs the inter-ELM profile slightly broadens. More importantly however, the power deposition zone during the ELM shrinks, whereas the peak power flux is reduced only by 7%. Despite of lower ELM-energies arriving at the target this could have an adverse effect on the energy density.

The changes of the power flux profile are mainly brought about by the particle flux (see figure 4). The inter-ELM profiles exhibit similar features as the power flux profiles: a narrow profile, which broadens during EFCCs. The profiles at the ELM-peak have a larger broadening compared to the power flux profile. Finally one should note that the strike point moves during the ELM, which in addition spreads the power load over a larger area. The strike point movements caused by the sudden loss of edge currents during ELMs have been discussed in [11].

Another concern for a bulk-tungsten divertor is the electron temperature in front of the target, which should be kept below 5eV in order to avoid tungsten sputtering. Due to the reduction of the upstream density and confinement one expects the target temperature to rise. Langmuir probe measurements have shown that in the unfuelled pulses the temperature profile shrinks (see figure 12) and its peak value rises form ~25 to ~40eV during the EFCC phase. With large fuelling however the target temperature can be lowered despite of the inherent density pump-out.

4. IMPLICATION OF ELM-ENERGY ON MATERIAL-LIMITS

As pointed out earlier the relevant quantity for the material-limit is the energy density and the heat flux factor ηELM. In earlier publication of the ratio of total energy arriving at the divertor target

over the wetted area when the power has reached its maximum has been used. However, as shown in figure 5, the wetted area, inferred from the total power $P_{tot}(t)$ over the maximum heat surface flux $Q_{surf}(t,R)$, is maximal after the ELM-peak. This has to be beard in mind when calculating the heat flux factor. In order to account for the temporal variation of the power wetted area and the strike point movement during the ELM we introduce a definition of the wetted area based on the energy density profile.

The energy density profile is derived by integrating at each radial position the heat flux profile $Q_{surf}(t,R)$ in time from the start of the ELM until the end, which is defined as two decay times after the peak in the total power, i.e. the energy density is

$$\varepsilon_{ELM}(R) = \int_{t_{start}}^{t_{end}} Q_{surf}(t,R)\, dt \tag{2}$$

with R as target coordinate. The blue curve in figure 5 shows the time trace of the surface heat flux during a typical ELM. The integration window is indicated by the red diamonds. The steady state heat flux during the ELM is estimated by an interpolation of the heat fluxes at the integration boundaries. Half of the resulting energy density is attributed to the ELM, the other half of to the inter-ELM value. Typical profiles of the energy density obtained with this method are shown in figure 6 for the same unfuelled with-EFCC and without-EFCC cases as shown earlier. One should note that the maximum of the profiles are slightly further outward compared to the heat flux profile, which is due to the strike point movement during the ELM.

In addition, the shrinking of the profile during the EFCC-phase is even more pronounced.

By integrating radially over the target using a toroidal wetted area fraction of 0.82, which is a good estimate for low q_{95}-plasmas, one can determine the total energy per ELM arriving at the target:

$$E_{ELM} = 2\pi R_0 \varepsilon_{wet} \int_{R_{in}}^{R_{out}} \varepsilon_{ELM}(R) dr \tag{3}$$

with R_0 as the radial position of the middle of the divertor tile. We define the wetted area during an ELM in the conventional way by the ratio of EELM over the maximum of the energy density profile ε_{ELM}:

$$A_{wetted} = E_{ELM} / \varepsilon_{ELM,\, max} \tag{4}$$

This quantity can be seen as an average wetted area during the ELM, taking into account possible strike point movement and the temporal evolution of the total power flux and maximum heat flux. Using equation (1) and (4) we see that the heat flux factor η_{ELM} is proportional to the maximum of the energy density profile:

$$\eta_{ELM} = \varepsilon_{ELM,\, max} / \sqrt{t_{dur}} \tag{5}$$

For the time duration the time difference corresponding to the integration times in Eq. (2) has been used. The inter-ELM wetted area has been determined in a similar fashion by replacing the integration boundaries by the tend of the last and tstart of the following ELM.

The compilation of the ELM-wetted area and inter-ELM wetted area from a large database containing ELMs from pulses with, without EFCCs, unfuelled and fuelling is shown in figure 7. For the unfuelled, unmitigated ELMs we notice an increase of the wetted area during the ELM (blue, open triangles) with respect to the inter-ELM values (blue, open squares) by a factor of four. With the application of gas fuelling the ELM-size can be reduced (blue, closed symbols) and concomitantly the inter-ELM wetted area slightly increases. The large scatter of the data at the ELM-peak (blue, closed triangles) prevents us to determine whether there is a change in the ELM-wetted area.

The mitigated ELMs have much lower energy. The most significant effect is that the inter-ELM area nearly doubles with respect to the unmitigated ELMs. The ELM-wetted area $A_{wet,ELM}$, however decreases with ELM-size. The combination of all data points for Awet,ELM indicates a linear-offset like dependence on ELM-size. The heat flux factor therefore changes with ELM-size as it can be seen in figure 8. There is a remarkable relation of η_{ELM} with ELM size represented by the ELM-energy arriving at the target EELM, which is the same for unmitigated, mitigated and gas-fuelled ELMs.

Besides the reduction of the pedestal pressure leading to smaller ELMs, there is no additional beneficial effect of ELM-mitigation using EFCCs compared to gas-fuelling. This can be further inferred from figure 9, where the heat flux factor has been plotted against the confinement factor H98. For both series of gas scans with and without EFCC, the heat flux factor decreases with confinement as the gas fuelling rate increases.

One can summarise the mechanism of ELM-mitigation as follow. The loss of edge density and concomitantly constant temperature leads to a degradation of the pedestal. This results on one hand in lower plasma energy and on the other hand to lower ELM-energies, which reduce the heat flux factor at the target. The degradation of the pedestal however can be also achieved by simple gas-fuelling.

In order to see, whether there is a threshold for ELM-mitigation, an experiment where the EFCC-current has been slowly ramped at a rate of 600A/sec has been carried out. The resulting change of η_{ELM} with ELM-frequency is shown in figure 11 (yellow symbols). In addition, the results from the gas-scans are added (blue and red squares). Least square fits applied separately to both datasets using a power law dependence revealed the following scaling for the reduction of η_{ELM} with increasing f_{ELM}: for the data obtained from the slow ramp of EFCC-current $\eta_{ELM} \propto f_{ELM}^{-0.27 \pm 0.02}$ and for the dataset corresponding to the gas scans $\eta_{ELM} \propto f_{ELM}^{-0.41 \pm 0.14}$. This is less favourable than an inverse linear scaling. For instance in order to achieve a reduction of the expected heat flux factor predicted for ITER of $600MJ/m^2/s^{-1/2}$ down to $40MJ/m^2/s^{-1/2}$, the ELM-frequency would have to be risen by a factor of 700.

5. EFFECT OF NITROGEN SEEDING ON ELM-IMPACT

Nitrogen (N_2) is an attractive candidate to increase the divertor radiation, which is expected to lower the steady state power loads to the divertor target and the electron temperature in front of the targets. In high triangularity plasmas ($\delta = 0.42$) at a plasma current of 2.5MA, toroidal field of 2.7T, q_{95} of 3.5 scans of deuterium gas fuelling (up to 2.8×10^{22}el/sec) and seeding rates (up to 4.7×10^{22} el/sec) have been carried out [7]. An analysis of the pedestal pressure profile revealed a degradation of the pedestal energy with increasing deuterium fuelling. If nitrogen is added the pedestal pressure degrades further. As a result, the heat flux factor is reduced in a similar fashion for pure D_2-fuelled (c.f. black symbols in figure 13) and N_2-seeded pulses (red symbols in Fig.13). Interestingly, pulses at very high N2-seeding rates (4.7×10^{22}el/sec) showed a pedestal degradation of about 35%, whereas ηELM dropped by a factor of 5. This is more visible in figure 14, where η_{ELM} is shown as a function of nitrogen seeding rate. Modest seeding of nitrogen has a similar effect as D_2-fuelling, i.e. some reduction of η_{ELM}. However, only with the largest N_2-seeding η_{ELM} decreases significantly. The Z_{eff} in these pulses were around 2.2. The confinement indicated by the $H_{98(y,2)}$-factor in the lower box of figure 14 was only reduced by about 20%.

CONCLUSIONS

The broadening of the power deposition profile and strike point movement during ELMs by a factor of 2 to 4 helps to reduce the power load caused by ELMs. The impact of the ELMs onto the divertor was characterised with the heat flux factor, which is proportional to the surface temperature rise. The wetted area has been analysed taking into account the strike point movement and profile broadening and has been seen to increase with ELM-size. The degradation of the pedestal, however, leads to smaller ELM-energy and the ELM impact is reduced. Similar degradation of pedestal and confinement has been found for mitigated ELMs using EFCCs, gas-fuelling and impurity seeding. Regarding the ELM-impact onto the divertor no advantage of using EFCCs over other methods, such as gas-fuelling or nitrogen-seeding, can be reported. A scaling of the heat flux factor with increasing ELM-frequency has revealed a weak dependence, i.e. the rate of change of η_{ELM} with ELM-frequency is lower than linear. Only very high nitrogen seeding rates have lead to a scenario, where the ELM-impact was significantly reduced with only a modest reduction of confinement.

ACKNOWLEDGEMENT

This work, supported by the European Communities under the contract of Association between EURATOM/Belgian State, was carried out within the framework of the European Fusion Development Agreement. The views and opinions expressed herein do not necessarily reflect those of the European Commission.

REFERENCES:

[1]. G. Federici, Plasma Physics and Controlled Fusion **45** (2003), 1523.

[2]. G. Matthews, these proceedings.
[3]. N. Klimov, Journal of Nuclear Materials **390-391** (2009), 721.
[4]. R. Pitts, these proceedings.
[5]. Y. Liang et al., Nuclear Fusion **50** (2010), 025013.
[6]. E. de la Luna et al., Proc. 36th EPS-conference (2009).
[7]. G. Maddison et al., these proceedings.
[8]. T. Eich et al., these proceedings.
[9]. W. Fundamenski et al., Plasma Physics and Controlled Fusion **44** (2002), 761.
[10]. S. Jachmich et al., Journal of Nuclear Materials **363-365** (2007), 1050.
[11]. E. Solano et al., Nuclear Fusion **48** (2008), 065005.

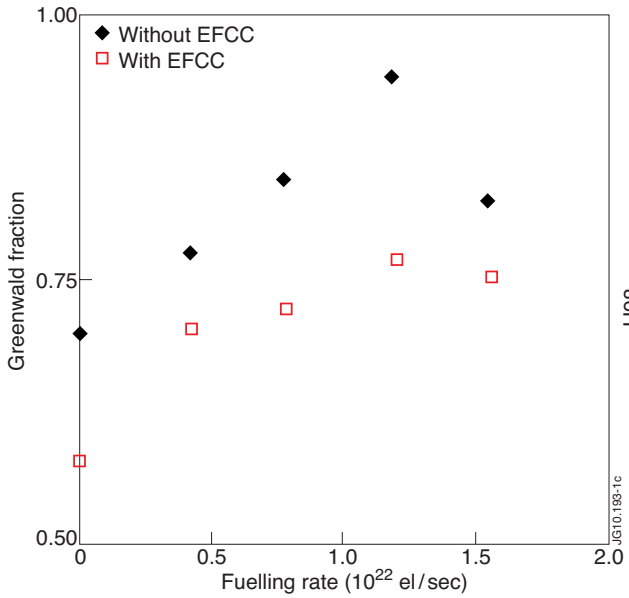

Figure 1: Greenwald density fraction versus fuelling rate from gas scans during phases with (red symbols) and without EFCCs (blue symbols).

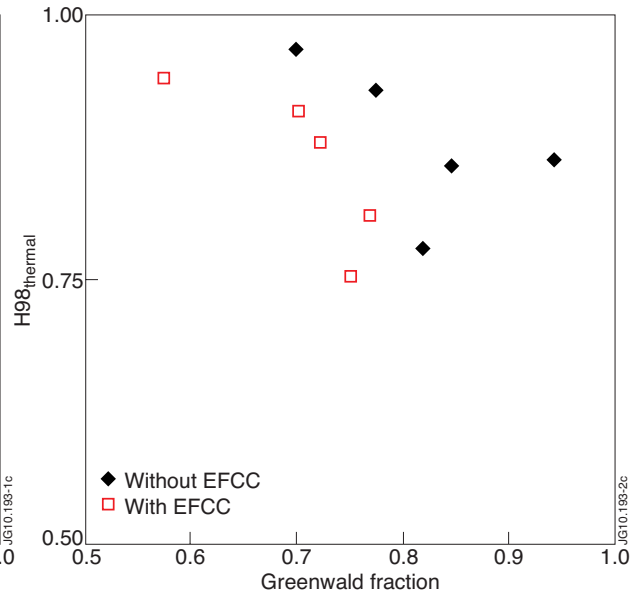

Figure 2: Confinement factor H98(y,2) versus Greenwald fraction.

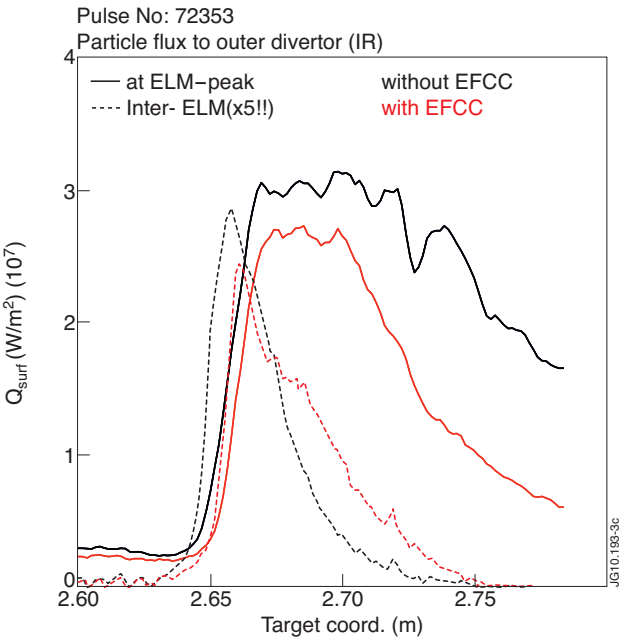

Figure 3: Heat flux profiles measured by IR taken at times at the ELM-peak (solid lines) and inter-ELM (dashed lines). Red curves and blue curves correspond to phases with and without EFCCs of an unfuelled discharge.

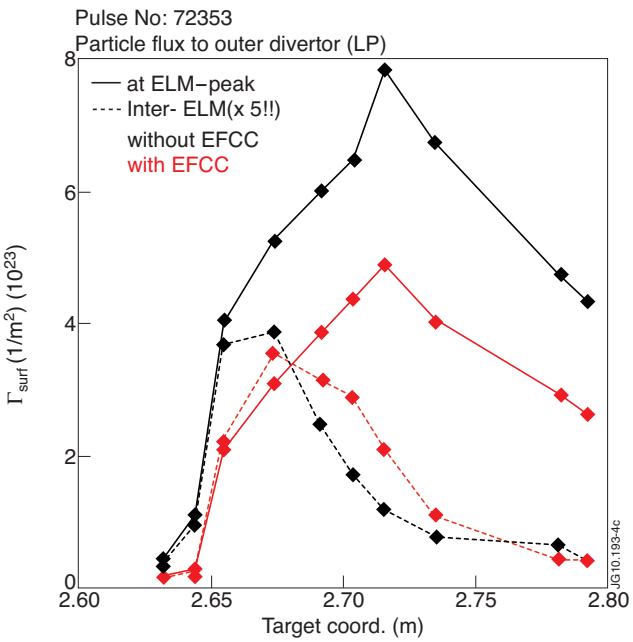

Figure 4: Particle flux profiles me asured by Langmuir probes at the ELM-peak (solid lines) and inter-ELM (dashed lines). Red curves and blue curves correspond to phases with and without EFCCs of an unfuelled discharge.

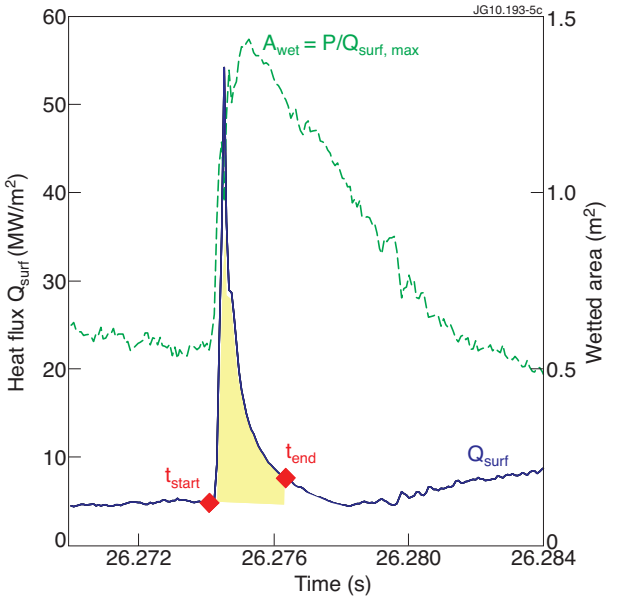

Figure 5: Time trace heat flux and wetted area (A_{wet} = P/Q_{max}) during an typical ELM. Note that the wetted area peak does not concide with the time when the maximum power is reaching the target.

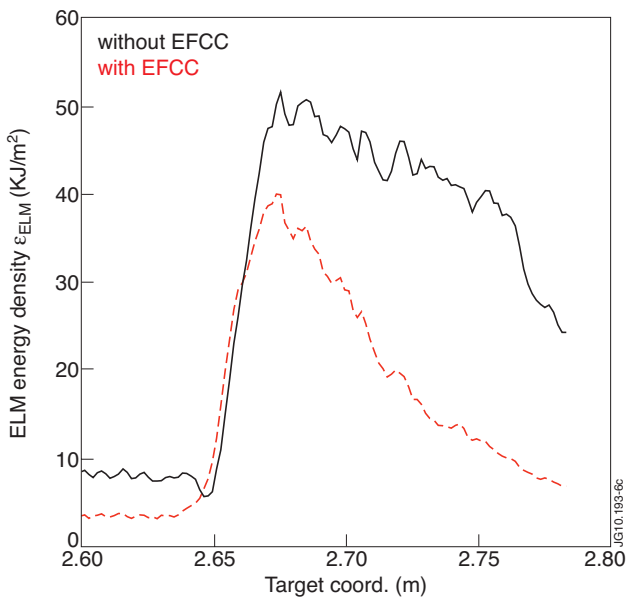

Figure 6: Profiles of energy density averaged over ELMs during phases with (red) and without (black) EFCCs.

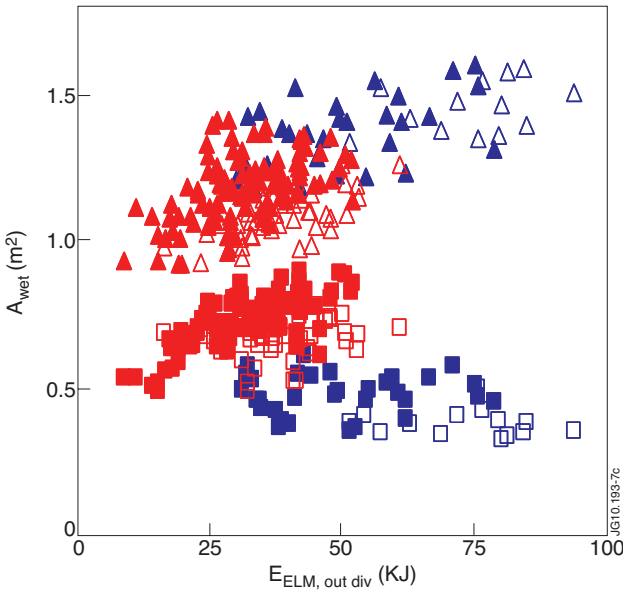

Figure 7: Wetted area as defined in Eq. (2) versus ELM energy arriving at the outer divertor target. The open symbols are corresponding to unfuelled phases, full to fuelled ones. The triangles are representing ELM-wetted area, the squares in between ELMs. Blue symbols are for without EFCCs and red ones are with EFCCs.

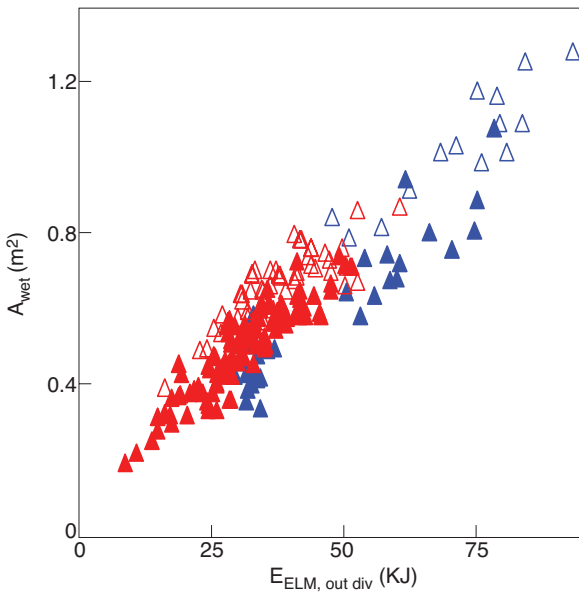

Figure 8: Heat flux factor as function of ELM-size for the same data set as in figure 7.

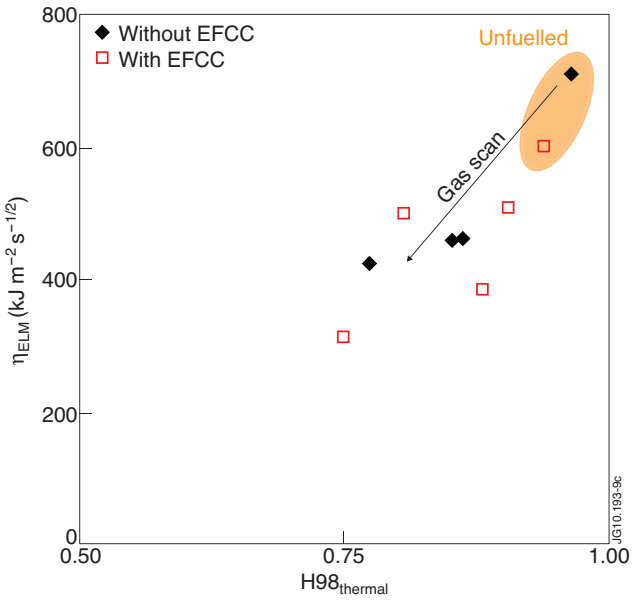

Figure 9: Heat flux factor versus confinement factor H98(y,2).

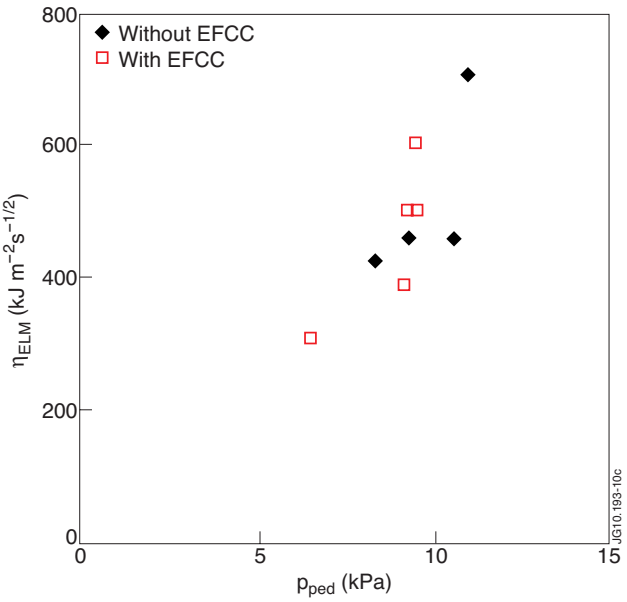

Figure 10: Heat flux factor versus pedestal pressure.

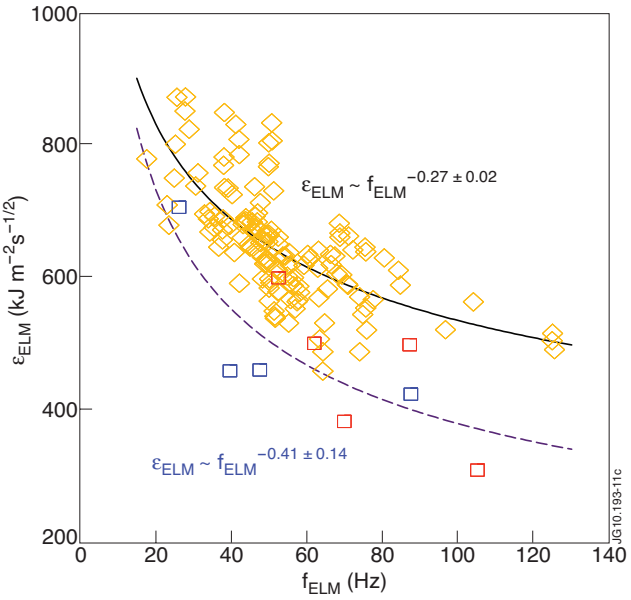

Figure 11: Scaling of heat flux factor with ELM-frequency. The solid lines represent the result of a least-square power law fit separately to the dataset of the slow EFCC-ramp and to the dataset of the gas-scan.

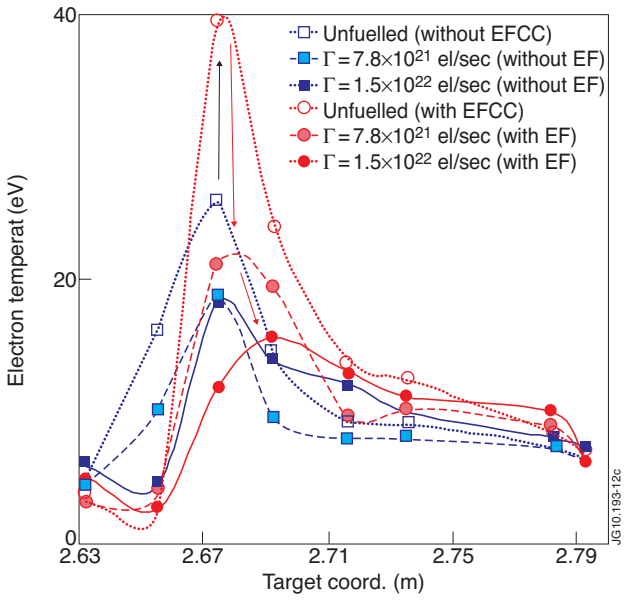

Figure 12: Target temperature profiles during EFCC (red) and no-EFCC (blue) reference phases at three fuelling levels: unfuelled (short dashes), Γ_{D2} = 7.8×10^{21} el/sec (long dashes), Γ_{D2} = 1.5×10^{22} el/sec (solid)

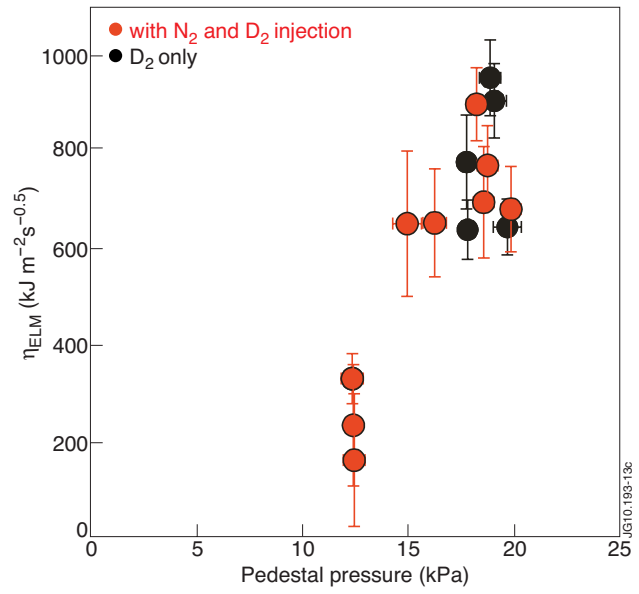

Figure 13: Effect of pedestal pressure on heat flux factor. The three lowest red points correspond to the highest N_2-seeding rate.

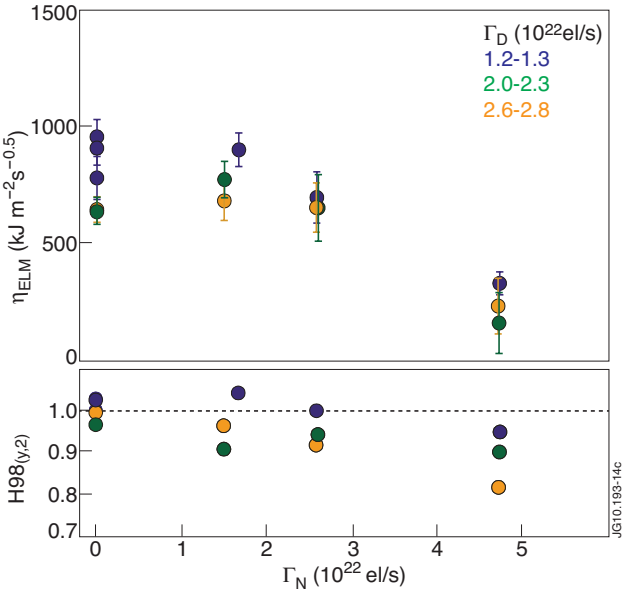

Figure 14: Heat flux factor for different deuterium fuelling (upper box) and resulting H98-factor (lower box) versus nitrogen seeding rate. The various colors indicate different ranges of D_2-fuelling.

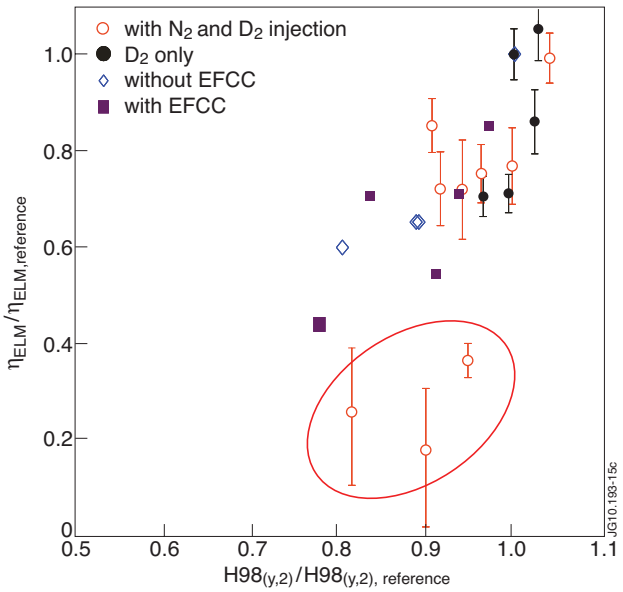

Figure 15: Normalised heat flux factor versus normalized confinement factor.